

# Deflectometry for measuring inhomogeneous refractive index fields in two-dimensional gradient-index elements

DI LIN,<sup>1,\*</sup> JEREMY TEICHMAN,<sup>2</sup> AND JAMES R. LEGER<sup>1</sup>

<sup>1</sup>Department of Electrical and Computer Engineering, University of Minnesota, Minneapolis, Minnesota 55455, USA

<sup>2</sup>Institute for Defense Analyses, Alexandria, Virginia 22311, USA

\*Corresponding author: linx0284@umn.edu

Received 5 February 2015; revised 29 March 2015; accepted 30 March 2015; posted 30 March 2015 (Doc. ID 233764); published 30 April 2015

We present a numerical method for calculating inhomogeneous refractive index fields in rectangular gradient-index (GRIN) elements from measured boundary positions and slopes of a collection of rays that transit the medium. The inverse problem is reduced to a set of linear algebraic equations after approximating ray trajectories from the measured boundary values and is solved using a pseudo-inverse algorithm for sparse linear equations. The ray trajectories are subsequently corrected using an iterative ray trace procedure to ensure consistency in the solution. We demonstrate our method in simulation by reconstructing a hypothetical rectangular GRIN element on a  $15 \times 15$  discrete grid using 800 interrogating rays, in which RMS refractive index errors less than 0.5% of the index range ( $n_{\max} - n_{\min}$ ) are achieved. Furthermore, we identify three primary sources of error and assess the importance of data redundancy and system conditioning in the reconstruction process. © 2015 Optical Society of America

**OCIS codes:** (080.2710) Inhomogeneous optical media; (120.3940) Metrology.

<http://dx.doi.org/10.1364/JOSAA.32.000991>

## 1. INTRODUCTION

Gradient-index (GRIN) materials belong to a class of inhomogeneous optical media whose refractive index varies with position. Myriad techniques have been studied for fabricating increasingly complex index variations [1,2]. In recent years, there has been increasing interest in exploring novel GRIN materials to develop compact, lightweight, and robust optics. Current methods for fabricating GRIN materials include neutron irradiation [3], chemical vapor deposition (CVD) [4], ion exchange [5,6], and variations of polymer-based processes [7–9]. The underlying physical principles behind these fabrication methods have always limited their ability to produce arbitrary index profiles. However, several new methods have been developed (e.g., Ref. [10]) that permit unprecedented control over the index profile in two and three dimensions.

GRIN materials are useful in a variety of applications; they offer appealing form factors as well as additional degrees of freedom (DoFs) in controlling the propagation of light. These materials have found application in telecommunications and compact imaging. For instance, their unique dispersion characteristics can be incorporated into optical fibers to reduce modal dispersion and thereby increase the bandwidth and repeater distance of optical communication systems [1]. In addition, the cylindrical form factor of GRIN optics simplifies coupling

between optical fibers and sources. The optical power of GRIN lenses is determined not only by their surface geometry but also by their refractive index distribution. By combining the two effects, new approaches to chromatic as well as spherical aberration correction become possible [11,12]. Furthermore, GRIN optics can be designed to redistribute irradiance in an optical beam and perform coherent mode conversion in beam shaping applications [13–15].

The refractive index profile of the GRIN material dictates the propagation of light inside the medium. Accurate knowledge of its index is therefore required for integration into optical systems. For one-dimensional (1-D) GRIN profiles, conventional methods of measuring the index utilize beam displacement or beam deflection to measure the index gradient. These methods are typically based on simplifying geometric assumptions [16–18] that become invalid when a significant amount of refraction occurs inside the sample. Interferometric methods that utilize fringe patterns for phase retrieval [19] are ambiguous without prior knowledge of the index field under investigation. In addition, resolving fringes becomes impractical when propagation distances inside the medium are substantial. Optical coherence tomography (OCT) has been shown to provide high-resolution imaging of layered GRIN profiles [20], but the principles behind this approach require scattering elements, such as discontinuities

in the index, inside the measured sample. In a previous study, we showed that boundary measurements of ray position and slope can be bootstrapped to ascertain the index profile of a thick 1-D GRIN element, provided the index is known at some initial location [21].

In the case of two-dimensional (2-D) GRIN profiles, straight ray trajectories assumed in tomographic approaches facilitate Fourier synthesis of the index field from interferometric data with the help of the projection slice theorem [22]. However, reconstruction accuracy is quickly compromised in the presence of even a modest refracting index field. In more recent studies, deflectometry principles have been utilized in interrogating weakly refracting index fields using x rays [23,24]. While ray trajectories can be approximated as linear in the x-ray regime, the refractive index of materials is generally significantly higher than unity for longer wavelengths and the medium cannot be assumed to be weakly refracting. Consequently, ray trajectories are seldom linear and the effects of Snell's law at discontinuities at interfaces cannot be ignored. Finally, although analytical solutions have been shown for deflectometry in specific geometries such as radially symmetric index profiles of optical fiber preforms [25], there has been no reported method of directly inverting deflectometry measurements for 2-D index fields in the general case.

In this study, we propose a method for calculating 2-D index fields in rectangular GRIN elements using boundary measurements of ray position and slope. We will first discuss the simplifying assumptions that enable us to formulate the inverse problem as a linear system in Section 2, where we use optical path length (OPL) measurements to explain the mathematical method in a simpler context. An extension of our formulation to deflectometry data will be detailed in Section 3, where we will establish the primary system of equations to be inverted. In Section 4, an implementation of the proposed method will be demonstrated in the reconstruction of a hypothetical index field, where deflectometry data are generated in simulation and the primary system equation is inverted using numerical methods. We will then identify the primary sources of error in the reconstruction process and outline a few practical numerical aspects of system inversion in Section 5. In Section 6, we will provide the justification for the assumptions made in Section 2 and demonstrate an iterative procedure to ascertain more accurate ray trajectories from boundary measurements. Finally, a conclusion and outlook for future work will be provided in Section 7.

## 2. LINEAR ALGEBRAIC SYSTEM FORMULATION

Determining an unknown 2-D index field through boundary measurements of ray position and slope is an inverse problem that can be described as a set of simultaneous algebraic equations in the DoFs in the system. The number of DoFs needed to represent the index field is associated with its space-bandwidth product [26]. Suppose that we discretize a 2-D index field  $n(x, y)$  using a uniform rectangular grid, as shown in Fig. 1, such that the index value at each sample point  $n_{l,k}$  represents an unknown in the system. In order to maintain generality for interpolation purposes, the unknowns of the system

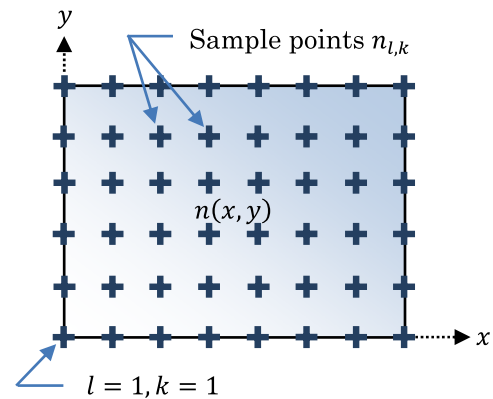


**Fig. 1.** Discrete representation of a 2-D index field using a uniform rectangular grid.

are treated as sample points rather than discrete rectangular elements.

With the help of a simplifying assumption, we will show that path integrals of the field quantity  $n(x, y)$  measured by individual interrogating rays can be expressed as algebraic equations in the unknowns of the system. For the sole purpose of illustrating the underlying principles in our method, suppose that interrogating rays propagating through the index field report the absolute OPL traveled along their trajectories from point  $a$  to point  $b$  in Fig. 2(a). This measurement can be expressed as the path integral

$$\varphi = \int_a^b ds \cdot n(x, y), \quad (1)$$

where  $\varphi$  is the total OPL and  $ds$  is the differential arc length along the ray path, as seen in the figure. In a low-order approximation scheme, Eq. (1) can be discretized in the form of a Riemann sum:

$$\varphi = \int_a^b ds \cdot n(x, y) = \sum_l \sum_k ds_{l,k} n_{l,k}, \quad (2)$$

where indices  $l, k$  correspond to a discrete rectangular region at laboratory coordinates  $(x, y)$  inside the index field. In this approximation, the index  $n_{l,k}$  is assumed to be constant within each region and  $ds_{l,k}$  represents the arc length for the ray segment inside the region, as shown in Fig. 2(b).

Multiple interrogating rays used to measure the index field in the form of Eq. (2) produce a set of algebraic equations. At present, these equations are nonlinear in  $n_{l,k}$  because the arc length  $ds_{l,k}$  depends on the trajectory of the interrogating ray, which in turn depends on the index field according to the ray equation of geometric optics [27],

$$\frac{d}{ds} \left( n \frac{d\vec{r}}{ds} \right) = \nabla n, \quad (3)$$

where  $ds$  is the arc length along the ray,  $\vec{r}$  is the position vector of a point along its trajectory, and  $n$  is the refractive index.

We argue that index fields in practical GRIN elements do not lead to large differences in ray trajectory as far as the local position and direction are concerned; any reasonable trajectory that satisfies the measured boundary values of position and

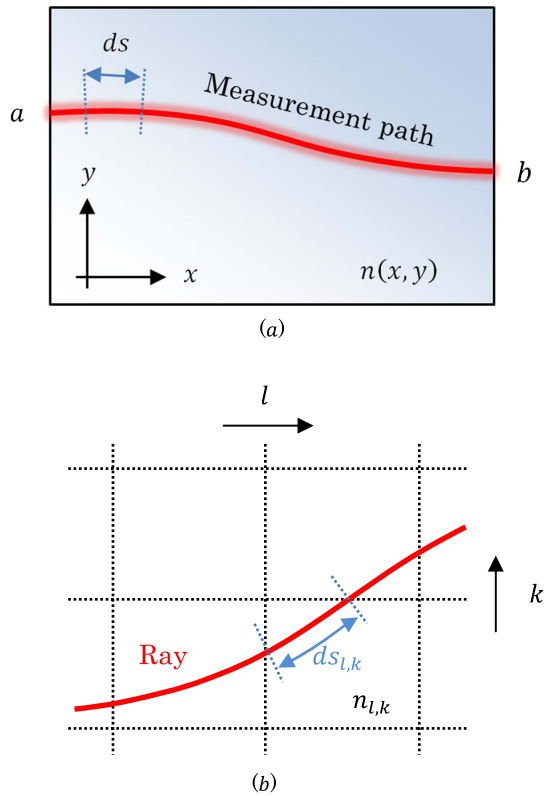


**Fig. 2.** Geometry of (a) deflectometry path integral measured by an individual interrogating ray and (b) the discrete approximation of that integral.

slope (e.g., a trajectory defined by a cubic polynomial) will exhibit enough similarity to the actual trajectory to be used as an approximation. Hence, we intend to ignore the dependence stated in Eq. (3) initially and construct approximate ray trajectories solely from measured boundary values of ray position and slope. This greatly simplifies the system because Eq. (2) becomes linear in  $n_{l,k}$  and the coefficients  $ds_{l,k}$  can be determined from these approximate trajectories. A sufficient number of measured rays will produce a set of simultaneous linear algebraic equations of the form

$$[S] \cdot \vec{n} = \vec{\varphi}. \quad (4)$$

In this equation,  $[S]$  is the system matrix containing all the discrete arc lengths from multiple measured rays, where each row of the matrix contains a lexicographically ordered (or raster scanned) version of the 2-D field shown in Fig. 2(b), with the elements of each row containing pieces of the arc length  $ds_{l,k}$  from a single measured ray traversing the field. The column vector  $\vec{\varphi}$  contains the OPL values associated with path integrals from each measured ray, and the vector  $\vec{n}$  contains all unknown values of  $n_{l,k}$  lexicographically ordered into a single column vector. In principle, we can solve for the unknowns using the inverse formula  $\vec{n} = [S]^{-1} \cdot \vec{\varphi}$ , provided that we have enough equations such that  $[S]$  is a full rank matrix. If we have more equations than the number of unknowns, then the system is overdetermined and can be solved in the least squares sense by invoking the formula  $\vec{n} = ([S]^T \cdot [S])^{-1} \cdot [S]^T \cdot \vec{\varphi}$ . Once an

initial estimate for the index field  $n_{l,k}$  has been obtained, an iterative ray trace procedure can be used to correct the approximate trajectories such that all final ray trajectories observe the relation in Eq. (3). This procedure is detailed in Section 6.

### 3. EXTENSION TO DEFLECTOMETRY

We have established above that path integrals in an unknown index field describing the *absolute OPL* traveled by a set of rays can be expressed as linear algebraic equations in the discrete sampled values of the index field. Similarly, the *angular deflection* of a set of interrogating rays can be expressed as path integrals of the index field's partial derivatives. Assuming ray trajectories are of the form  $y = y(x)$ , Eq. (3) can be rewritten as (see Appendix A)

$$\frac{\partial w}{\partial y} - \frac{\partial w}{\partial x} y' = \frac{y''}{1 + (y')^2}, \quad (5)$$

where  $w(x, y) = \ln[n(x, y)]$  is the logarithmic index and the prime symbol denotes differentiation with respect to  $x$ . It is straightforward to show from Eq. (5) that the normal component of the local index gradient induces a change in the ray's direction (see Appendix B), such that the differential angular deflection is given by

$$d\theta = \nabla w \cdot \hat{n} \cdot ds = \left[ -\frac{\partial w}{\partial x} \sin(\theta) + \frac{\partial w}{\partial y} \cos(\theta) \right] ds, \quad (6)$$

where  $\hat{n} = -\sin(\theta)\hat{i} + \cos(\theta)\hat{j}$  is the normal unit vector to the ray and  $\nabla w = \frac{\partial w}{\partial x}\hat{i} + \frac{\partial w}{\partial y}\hat{j}$  is the gradient of the logarithmic index field  $w(x, y)$ . Hence the total angular deflection accumulated over the entire trajectory of an interrogating ray from point  $a$  to point  $b$  can be expressed as a path integral of two distinct field quantities,

$$\Delta\theta = \int_a^b ds \cdot \left[ -\frac{\partial w}{\partial x} \sin(\theta) + \frac{\partial w}{\partial y} \cos(\theta) \right]. \quad (7)$$

Equation (7) is the analog of Eq. (1) for deflectometry measurements; it is the mathematical description of the measured interrogating ray in Fig. 3, provided that ray slopes are reported at  $a$  and  $b$  and the trajectory  $y(x)$  is known. In analogy with Eq. (2), Eq. (7) can be represented in discrete form (in a low-order approximation) as the Riemann sum

$$\Delta\theta = \int_a^b ds \nabla w(x, y) \cdot \hat{n} = \sum_l \sum_k ds_{l,k} \nabla w_{l,k} \cdot \hat{n}_{l,k}, \quad (8)$$

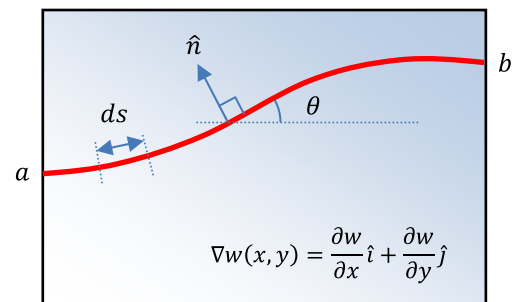


**Fig. 3.** Geometry of interrogating rays in two-dimensional deflectometry.

where indices  $l, k$  correspond to a discrete rectangular region at laboratory coordinates  $(x, y)$  on a rectangular grid representing the index field. In this approximation, the gradient vector  $\nabla w_{l,k}$  is assumed to be constant within each rectangular region;  $ds_{l,k}$  represents the arc length for the ray segment inside each region, and  $\hat{n}_{l,k}$  is taken to be the mean normal unit vector for this ray segment. As before,  $ds_{l,k}$  is obtained from approximate trajectories generated from measured boundary values such that Eq. (8) remains linear in  $\nabla w_{l,k}$ .

At first glance, it appears that Eq. (8) contains twice the number of DoFs as Eq. (2), as it contains two distinct field quantities sampled on the same grid. However, these field quantities correspond to the partial derivatives of an underlying scalar potential function and hence must satisfy

$$\nabla \times \nabla w = \frac{\partial}{\partial y} \frac{\partial w}{\partial x} - \frac{\partial}{\partial x} \frac{\partial w}{\partial y} = 0. \quad (9)$$

The vanishing curl in Eq. (9) ensures that  $w(x, y)$  is single-valued; any gradient field  $\nabla w = \frac{\partial w}{\partial x} \hat{i} + \frac{\partial w}{\partial y} \hat{j}$  with nonzero curl is unphysical. Computationally, Eq. (9) reduces the number of DoFs by a factor of 2. Given  $M$  sample points used to describe each partial derivative field, Eq. (9) produces  $M$  constraints. This means that, in principle, only  $M$  interrogating rays are needed to fully determine both  $\frac{\partial w}{\partial x}$  and  $\frac{\partial w}{\partial y}$ .

Writing Eq. (8) more explicitly, we have

$$\Delta\theta = \sum_l \sum_k ds_{l,k} \left[ -\frac{\partial w}{\partial x} \Big|_{l,k} \sin(\theta_{l,k}) + \frac{\partial w}{\partial y} \Big|_{l,k} \cos(\theta_{l,k}) \right], \quad (10)$$

where  $\theta_{l,k}$  is the average ray angle relative to the laboratory  $x$  axis in each rectangular region. The accuracy of the discrete approximation to Eq. (7) can be improved significantly by using higher-order interpolation schemes and invoking the trapezoidal rule of integration. The constraints in Eq. (9) can be discretized in the form

$$\left( \frac{\partial w}{\partial x} \Big|_{l,k+1} - \frac{\partial w}{\partial x} \Big|_{l,k} \right) - \left( \frac{\partial w}{\partial y} \Big|_{l+1,k} - \frac{\partial w}{\partial y} \Big|_{l,k} \right) = 0. \quad (11)$$

Notice that Eq. (11) does not apply to all sample points and produces only  $(L-1) \times (K-1)$  constraints if  $L \times K$  is the total number of sample points ( $M$ ). In practice, however, the number of measurements needed to accurately invert the system is significantly larger than  $L \times K$  and the deficit resulting from the finite-element implementation in Eq. (11) does not generally cause a problem in the inversion process. The redundant measurements also help suppress error contributions from individual measurements, which we will examine in detail in Section 5. Combining the path integrals from Eq. (10) and the constraints in Eq. (11) results in a set of simultaneous linear algebraic equations of the form

$$[S] \cdot \vec{\delta} = \vec{P}, \quad (12)$$

where the unknown vector  $\vec{\delta}$  now contains  $2(L \times K)$  sampled values, of which half describe  $\frac{\partial w}{\partial x} \Big|_{l,k}$  and the other half specify  $\frac{\partial w}{\partial y} \Big|_{l,k}$ . Letting  $N$  be the number of measured rays,  $N$  equations representing the deflectometry path integrals in Eq. (10) are

augmented by an additional  $(L-1) \times (K-1)$  equations corresponding to the irrotational constraints from Eq. (11) such that the total number of rows in  $[S]$  and  $\vec{P}$  is equal to  $N + (L-1) \times (K-1)$  in the final construction of the 2-D deflectometry system. The first  $N$  elements in  $\vec{P}$  correspond to angular deflection values, while the remaining spots are filled with zeros in accordance with Eq. (11). Equation (12) is the analog of Eq. (4) for deflectometry measurements and can, in principle, be inverted to obtain the gradient vector field  $\nabla w_{l,k}$ . Upon integrating  $\nabla w_{l,k}$ , the index field is specified up to an unknown constant, which can be identified with a single independent measurement of the refractive index, e.g., along the boundary.

#### 4. NUMERICAL DEMONSTRATION OF MEASUREMENT PROCEDURE

We demonstrate the efficacy of our method by applying it to computer-generated deflection data. This has the advantage of allowing us to measure the intrinsic accuracy of the numerical method separate from the measurement noise. The effects of measurement noise will be discussed in Section 5. We start by describing how deflection data are generated and then apply the method described in Section 3 in a step-by-step procedure.

##### A. Generating the Test Data

We began with an assumed index distribution shown in Fig. 4(a). The units along  $x$  and  $y$  in the figure are arbitrary provided that we use the same unit of measure for both spatial variables. We then utilized a numerical ray trace method based on the Eikonal equation [28] to generate boundary values for ray position and slope at the exit face of the rectangular index field for all rays applied to the entrance face. The ray trace provides interrogating ray trajectories that connect all possible pairings of entry and exit points, which are distributed uniformly along  $y$ . Figure 4(b) illustrates a set of interrogating rays that connect one particular entry point to all possible exit points. In the actual simulation, 20 entry points and 20 exit points were used to generate 400 interrogating rays.

We note that inverting the system using a family of interrogating rays that range primarily from left to right will likely produce highly inaccurate reconstructions of the index field due to poorly distributed sampling of the partial derivative fields. In particular, the sample points near the top and bottom boundaries of the field quantities are sampled by very few interrogating rays. Furthermore, it is evident from Eq. (8) that the index gradient component lying normal to the ray trajectory is responsible for the local angular deflection of the ray. Since the predominant direction of propagation is horizontal for the set of interrogating rays launched from the left-hand side of the GRIN element, these rays do not provide adequate sampling of  $\frac{\partial w}{\partial x}$ . In order to rectify this issue, we require a second set of rays propagating between the top and bottom boundaries of the rectangular index field. Thus, 20 entry points and 20 exit points uniformly distributed along  $x$  are used to generate 400 additional interrogating rays in a similar fashion, increasing the total number of measured rays to 800.

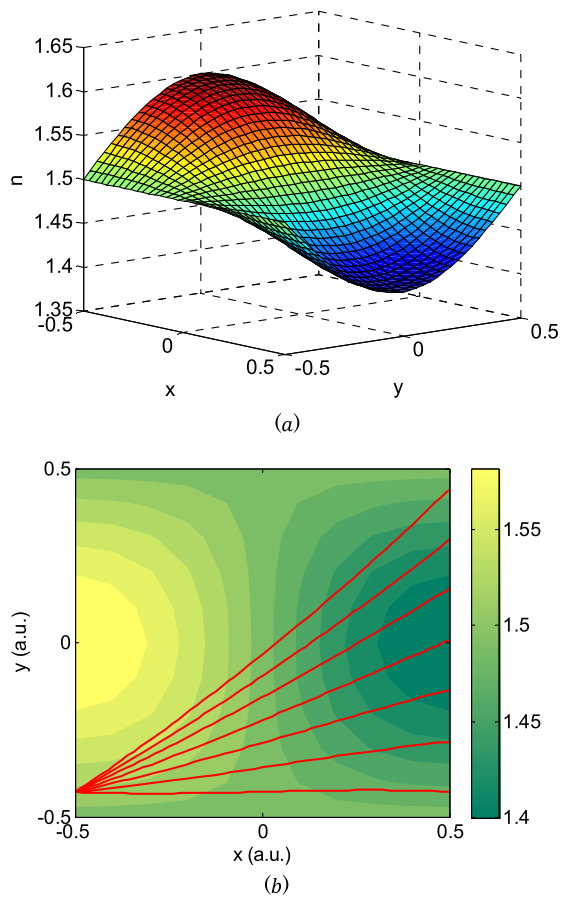


**Fig. 4.** (a) 3-D plot of the test index field used to generate boundary values of ray position and slope (resolution used in the numerical ray trace is  $35 \times 35$ ) and (b) sample interrogating ray trajectories obtained from the ray trace connecting one entry point to all possible exit points (reduced number of exit points are displayed in the plot for illustration purposes).

We then applied Snell's law to the calculated boundary values of ray position and slope inside the GRIN medium resulting from the ray trace to obtain the corresponding external boundary conditions that would be measured in an actual experiment. Assuming free space as the ambient medium, any interrogating ray that exceeded the critical angle for total internal reflection at the boundaries was discarded from our measurements. The ray locations and external slopes, as well as the index of refraction along the boundary, were subsequently used as input data for our recovery algorithm.

## B. Recovering the Index of Refraction

An outline of the overall procedure for calculating the index field from boundary values of ray position and slope is provided below, where it is understood that the index field and its gradient have been discretized on a rectangular grid and the rays used to interrogate the medium cover all grid points. Within this scenario, we proceed as follows:

1. Measure the index of refraction on the boundary using, e.g., a refractometer.

2. Measure the exit location and angle of a family of probe laser beams introduced at specific entrance locations and angles.

3. Ascertain internal ray slopes along the entrance and exit boundaries of the medium using Snell's law.

4. Construct approximate ray trajectories from internal boundary values.

5. For each ray trajectory, derive the corresponding path integral as an algebraic equation in  $\frac{\partial w}{\partial x}$  and  $\frac{\partial w}{\partial y}$ , where  $w = \ln[n(x, y)]$ , and  $n$  is the 2-D index of refraction we seek.

6. Assemble the algebraic equations into a linear system and augment the system with curl equations from the irrotational constraint of a conservative gradient field.

7. Invert the overall system equation to solve for  $\nabla w$  and integrate to obtain the index field.

In our computer-based test, step 1 is replaced by using the assumed boundary value data, and step 2 is replaced by using the calculated ray location and external slope data described in Section 4.A. Step 3 then consisted of applying Snell's law at the entrance and exit boundaries to ascertain the internal boundary values for rays that could be measured externally.

After defining the partial derivative fields on a  $15 \times 15$  grid, we used cubic polynomials to construct approximate ray trajectories according to step 4. We then derived the discrete expressions corresponding to the deflectometry path integral for each interrogating ray in step 5. In our discretization of Eq. (7), the partial derivatives of the logarithmic index field were obtained via constrained cubic spline interpolation, and numerical integration was carried out using the trapezoidal rule. The resulting expression for each path integral was considerably more complicated than the low-order approximation shown in Eq. (10). These methods were necessary to mitigate the quantization effects introduced into our model, as a low-order approximation will often lead to large discrepancies between generated deflection values and those calculated from the solution. Augmenting these equations with the irrotational constraints from Eq. (11) in step 6, we constructed the overall deflectometry system expressed in Eq. (12).

In principle, computing the inverse or the pseudo-inverse of  $[S]$  will enable us to compute the partial derivative fields we seek. In practice, however, solving for the partial derivative fields is more complicated than a direct inversion of  $[S]$ . Due to the similarity in the system coefficients generated in adjacent interrogating rays, the deflectometry system matrix  $[S]$  is inherently ill-conditioned. In addition,  $[S]$  is sparse because only a small set of sample points pertain to individual path integrals. These factors generally make the direct inversion of  $[S]$  unreliable due to numerical instability. The method of least squares QR factorization (LSQR), on the other hand, provides a far more reliable approach that is well-suited for solving sparse linear equations. While similar to other iterative numerical inversion techniques, it has been shown to be more reliable when the system matrix is ill-conditioned [29]. Furthermore, the LSQR method will optimize a solution in the least squares sense if the system is overdetermined. In the current and all subsequent simulations, the LSQR method will be employed for system inversion once  $[S]$  has been determined in Eq. (12).

The partial derivative fields obtained from the system inversion in step 7 and the resulting gradient vector field are shown in Fig. 5. These partial derivative fields were integrated

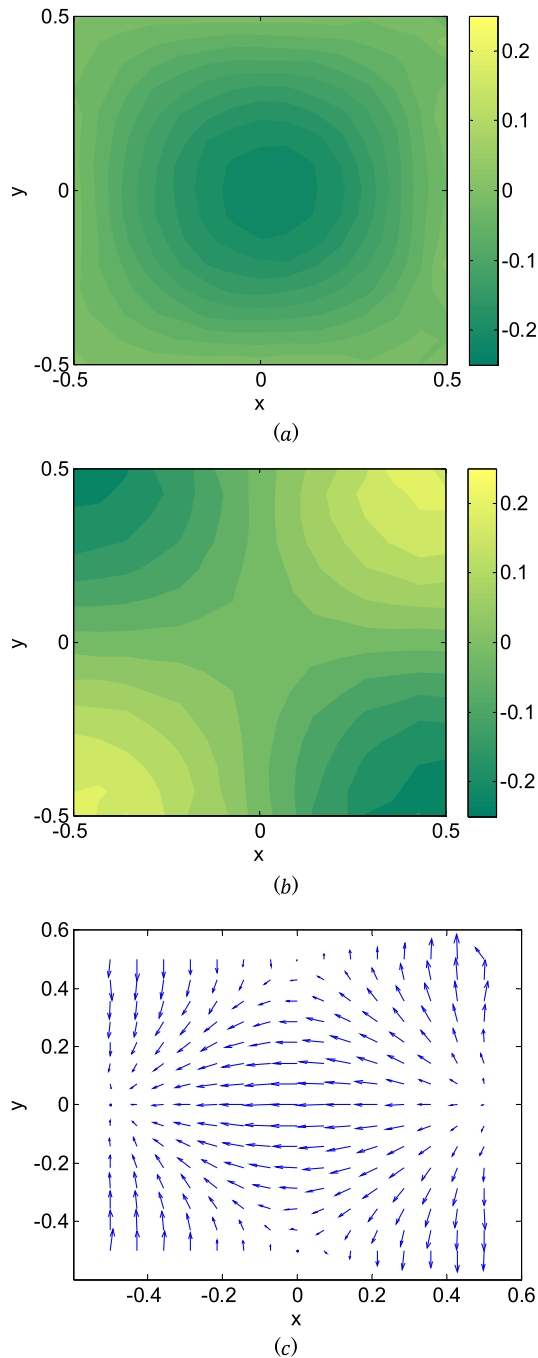


**Fig. 5.** Contour plots of reconstructed fields for (a)  $\frac{\partial w}{\partial x}$  and (b)  $\frac{\partial w}{\partial y}$  on a  $15 \times 15$  grid and (c) resulting gradient vector field  $\nabla w$ .

(see Appendix C) to obtain the potential function  $w(x, y) = w_1(x, y) + w_0$ , where  $w_0$  is the integration constant determined from the boundary index values obtained in step 1 of the procedure. We illustrate the reconstructed index field in Fig. 6, where the RMS error in the refractive index is  $7.67 \times 10^{-4}$  refractive index units, less than 0.5% of the total index range ( $n_{\max} - n_{\min}$ ).

The strong agreement between our reconstruction and the test index field from Fig. 4(a) suggests that the inversion process is relatively insensitive to small variations in the ray trajectories

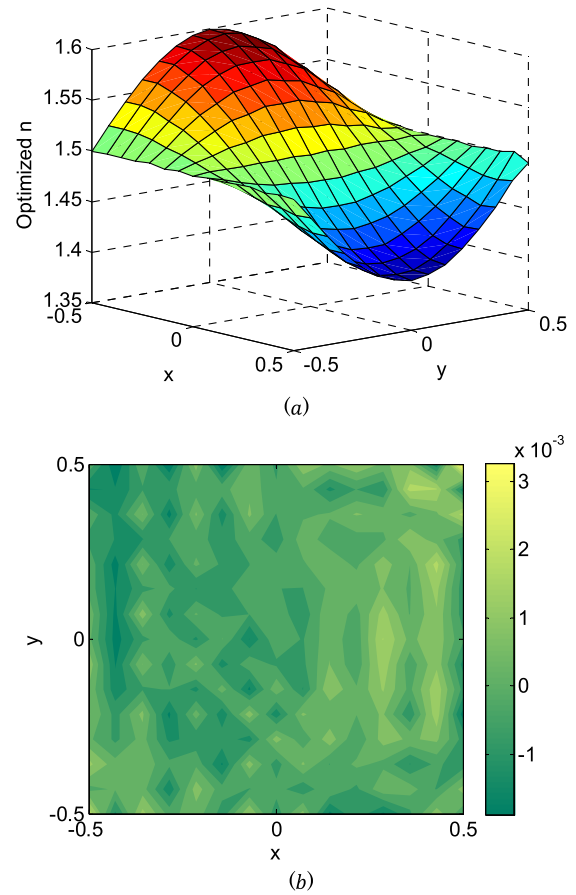


**Fig. 6.** (a) Reconstruction of the test index field after integrating the field quantities from Fig. 5 and (b) index error relative to the test index field from Fig. 4(a), with an RMS value of  $7.67 \times 10^{-4}$  refractive index units.

associated with individual rays. It stands to reason that the coefficients in  $[S]$  remain relatively static when ray trajectories are perturbed, at least in the case of slowly varying index fields. Hence, the discrepancies between approximate ray trajectories and those obtained from a ray trace through the actual index distribution are expected to be extremely small. We will take advantage of this feature to make corrections to the approximate ray trajectories in Section 6.

Upon closer examination of the reconstructed plots, we note that the errors are particularly high in the corner regions of the GRIN medium in both Figs. 5 and 6. This is primarily due to the reduced quality of interpolation near boundary sample points, which is exacerbated in the corner regions, resulting in a poor representation of the associated sample points in the discretized deflectometry path integrals.

## 5. RECONSTRUCTION ERROR ANALYSIS

We have so far demonstrated that an unknown index field can be accurately reconstructed from approximate trajectories using our proposed method. In the ensuing analysis, we identify three primary sources of error that contribute to the error in the reconstructed index field and characterize the conditioning of the system based on measurement parameters.

### A. Quantization Error

In order to model experimental measurements, deflection values for interrogating rays were generated through simulation using Euler's method for tracing rays [28] as described in Section 4.A. The quantization effects associated with this process introduce random noise to the calculated boundary values of ray slope and ray position. For this reason, a higher resolution was used for the discrete representation of the test index field during the initial ray trace than during the reconstruction process. Furthermore, the step size in Euler's method was chosen to reduce the quantization noise in the deflectometry data to a negligible level. When we apply these data to the system inversion procedure, the quantization noise introduced by the ray trace is analogous to experimental measurement error. Of course, these quantization effects are not present in an actual experiment and the error in the boundary values of ray slope and ray position is entirely dictated by measurement accuracy.

In addition to the quantization error associated with the generated deflectometry data, there exists a second type of quantization error of a different nature that also contributes to the reconstruction error observed in Section 4.B; the latter is associated with the discretization of the deflectometry path integral and acts independently of measurement error. This contribution depends on the quality of interpolation used in obtaining the quantities involved in the integral, namely,  $ds_{l,k}$  and  $\theta_{l,k}$  in Eq. (10) or analogous parameters in similar discrete expressions of Eq. (7) employing higher-order interpolation schemes. Moreover, the numerical integration technique used to discretize Eq. (7) also plays a role. In principle, one can always increase the grid resolution of the system to reduce the overall reconstruction error to an arbitrarily low value, provided that the geometric assumptions in Appendix B hold. However, doing so increases the DoFs in the system, and accurate inversion will require more measurements (interrogating rays).

### B. Measurement Error

In order to study the effects of measurement error on the reconstruction process, we introduced white Gaussian noise to the calculated boundary values (on top of the base-line quantization noise present in the ray trace used to generate the boundary values) prior to system inversion. As a preliminary test, we computed  $[S]$  in the deflectometry system equation based on cubic ray trajectories that fit the noise-free deflectometry data.  $[S]$  was left unchanged, while the values in  $\vec{P}$  corresponding to the total deflection of ray slope in the index field were subsequently contaminated with Gaussian noise. All other parameters were unchanged from the reconstruction in Figs. 5 and 6. This test allowed us to quantify the base-line inversion sensitivity of the linear system to measurement noise. Our results showed that the RMS index error in the reconstruction increased linearly with the Gaussian noise level, characteristic of a direct inversion of any linear system. This is seen in Fig. 7, where each data point represents the ensemble average over 100 trials of the simulation.

It follows that the base-line inversion sensitivity is related to the amount of data redundancy used in inverting the system. In theory, the minimum number of interrogating rays is equal to the number of DoFs in the system. In practice, however, any

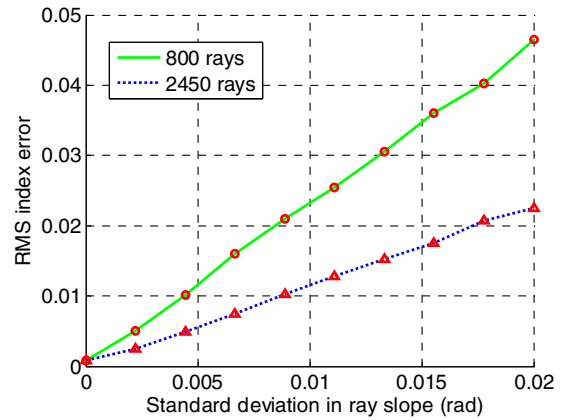


**Fig. 7.** Index error resulting from contaminated angular deflection values under different data redundancy conditions, where system coefficients are unaffected by the contamination.

measurement error or quantization error (in simulated measurements) in the boundary values can be greatly amplified in the reconstruction process. When used in conjunction with inversion methods that optimize the solution in the least squares sense, redundant measurements reduce the effect of error contributions from individual measurements by averaging over more samples, provided that the errors from different measurements are uncorrelated. In Section 4, we used approximately 800 deflectometry path integrals and almost 200 additional irrotational constraints to specify two discrete partial derivative fields consisting of 450 DoFs in total.

In a similar test, we increased the amount of data redundancy used during system inversion by changing the total number of interrogating rays to 2450. Plotting the resulting RMS index error for the same noise levels, the linear scaling factor between the noise level and the index error is seen to vary inversely with the amount of data redundancy, which we show in Fig. 7. The minimum RMS index error at the very left of the plot corresponds to the reconstruction error observed in Section 4.B and is due to the quantization effects discussed in Section 5.A.

In a more realistic model, the coefficients in  $[S]$  must be modified in accordance with the contaminated boundary values as they are generated from approximate trajectories that change with the measured boundary conditions. As before, the deflection values in  $\vec{P}$  are also subjected to the contamination. A subsequent simulation incorporating these perturbations in both  $[S]$  and  $\vec{P}$  after contaminating only boundary ray slope values at the exit reveals this dependence to be super-linear at high noise levels. This super-linear contribution to the index error is attributed to the path dependence of  $[S]$  and becomes negligible for low noise levels, as is evident from Fig. 8(a). For this simulation, we reduced the total number of interrogating rays to 450 and reconstructed the index field along with its partial derivative fields on an  $11 \times 11$  grid in order to make the super-linear contribution more apparent.

Unlike boundary slope values, uncertainty in boundary values of only ray position does not have any impact on  $\vec{P}$  and only affects the coefficients in  $[S]$ . As a result, its contribution to the

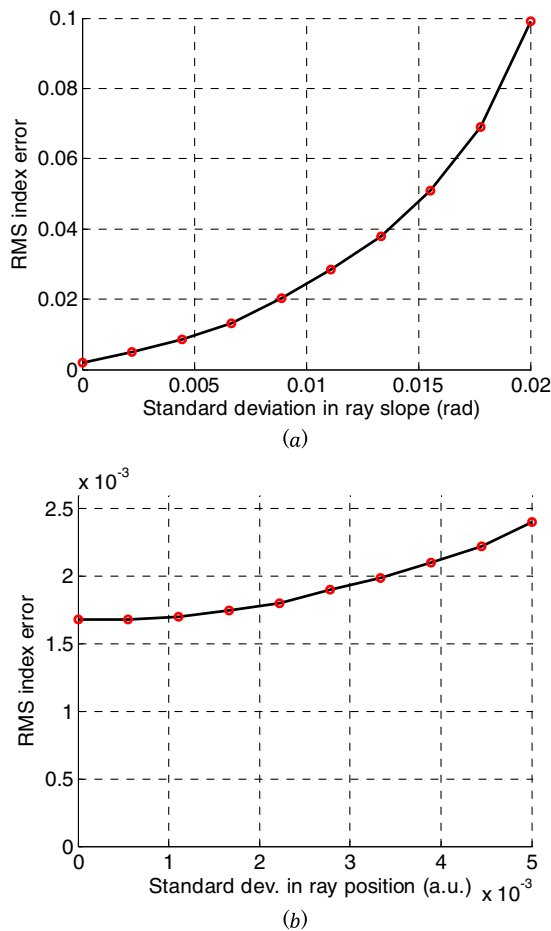


**Fig. 8.** Reconstruction error in index due to contaminated boundary values of (a) ray slope and (b) ray position at the exit.

reconstruction error is small compared to the error resulting from noise in the ray slope. This is apparent in Fig. 8(b), where the majority of the index error can be attributed to quantization effects. However, because the noise in the boundary ray positions affects the trajectories of the deflectometry path integrals in our model, we still expect its contribution to the overall reconstruction error to be super-linear.

To summarize, the reconstruction error resulting from system inversion can be attributed to three primary sources. At extremely low measurement noise levels, quantization noise becomes the major contributor. In an actual experiment, the quantization noise is limited to interpolation and integration error incurred in the process of discretizing Eq. (7). If the deflectometry data are generated through simulation, then the quantization error incurred during the initial ray trace also plays a role. At moderate noise levels, the base-line sensitivity in inverting a linear system is dominant while the super-linear contribution from the path dependence of  $[S]$  becomes significant at extremely high noise levels.

### C. System Conditioning

In order to gain a better understanding of the limitations of the LSQR method, it is useful to examine the numerical aspects of system inversion through its conditioning. Conditioning

measures the sensitivity of a system's output to small changes in its input. In our context, the input corresponds to measured boundary values of ray position and ray slope while the system's output is the reconstructed index field. As before, we can improve the system's conditioning through the use of data redundancy. While the difference between the plots in Fig. 7 clearly illustrates this reduction in sensitivity to measurement error, a more thorough characterization of data redundancy's impact on reconstruction accuracy is seen in Fig. 9(a), where we reduced the number of interrogating rays used in the reconstruction process without introducing artificial noise to the deflectometry data.

Angular coverage of the chosen family of interrogating rays also plays an important role in the conditioning of our deflectometry system. Figure 9(b) illustrates the impact of reducing angular coverage on reconstruction accuracy, where interrogating rays are omitted from the reconstruction process if their internal angles at either end exceed a threshold value. Once again, no artificial noise is introduced into the system in this simulation. There are no improvements beyond  $45^\circ$  in the figure because this is the absolute maximum angle allowed for interrogating rays propagating between opposite boundaries of the GRIN element due to its geometry.

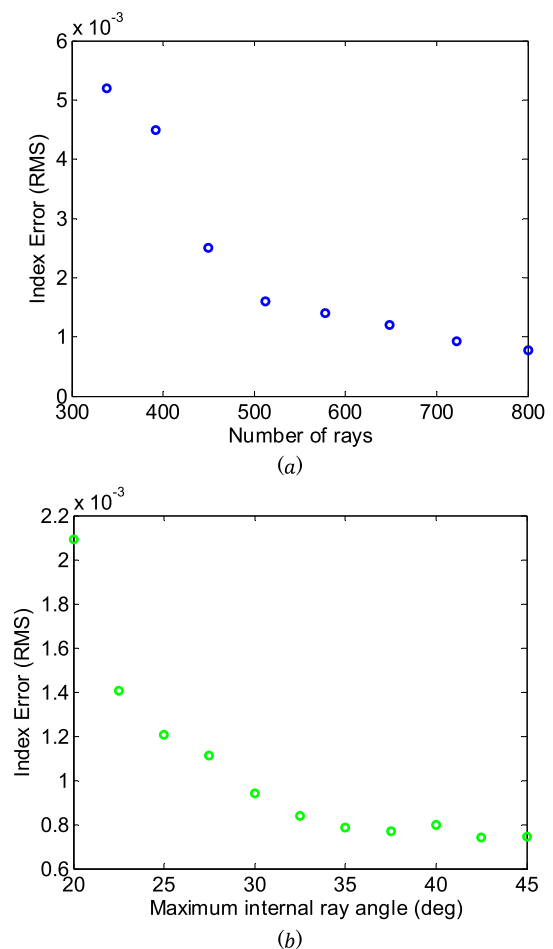


**Fig. 9.** Reduced reconstruction accuracy resulting from (a) reduced data redundancy and (b) limited angular coverage of interrogating rays.

Figure 9(b) explains why we were able to accurately reconstruct the test index field of Fig. 4(a) using the chosen set of interrogating rays. This result also holds implications for reconstruction accuracy based on the aspect ratio of the GRIN element. More specifically, the large angles required for accurate results may be difficult to achieve in GRIN elements with large aspect ratios. Furthermore, one must keep in mind the restrictions imposed by total internal reflection conditions at discontinuities along the boundaries of the GRIN element; it is possible that prism coupling or immersion in a fluid may be needed to access specific internal angles.

Both plots in Fig. 9 appear to indicate threshold values along the horizontal axis below which a significant increase in reconstruction error occurs. This increase is primarily due to the numerical instability of the LSQR method in the inversion of extremely ill-conditioned systems. We hasten to add that these characterization plots for conditioning are specific to the test index field in Fig. 4(a). Generally speaking, the requirements for data redundancy and angular coverage will depend on the complexity of the index field under investigation. For instance, an index profile whose gradient field is aligned in one direction would require significantly less angular coverage, provided that the rays used to interrogate the medium propagate predominantly in a direction that is perpendicular to the gradient.

## 6. CORRECTIONS TO RAY TRAJECTORIES

In Section 4, we hinted at the insensitivity of the inversion process to small variations in ray trajectories associated with individual interrogating rays. This was also apparent in Section 5, where extremely high measurement noise levels in measured boundary values were needed for the system's path dependence to manifest in the error plots. Despite the strong agreement we were able to achieve in our reconstruction of the test index field from Fig. 4(a), the solution is still fundamentally flawed as it is based on a set of ray trajectories that do not obey the ray equation of geometric optics. In this section, we show that successively refining the ray trajectories using an iterative ray trace procedure will eventually arrive at a consistent solution where the reconstructed index field reproduces the ray trajectories assumed in the reconstruction process. In other words, the trajectories obtained from ray tracing through the calculated index field  $w_{l,k}$  will produce the path-dependent parameters assumed in computing [S].

In the following simulation, the initial reconstruction of the index field from Fig. 6(a) is used as a starting point for our corrective procedure. Two separate ray traces are performed for each interrogating ray to improve the approximation to its trajectory. In one instance, the ray is launched with initial conditions associated with its entry point and is propagated toward its exit point; in the other, a ray is launched in reverse with initial conditions associated with the exit point. A weighted sum of the two similar trajectories is computed to ensure that the refined trajectory satisfies the measured boundary values at both ends, where the weighting coefficients start at unity at the launching point of the trace and decay linearly to zero as the trace approaches its terminating point. Upon obtaining new ray trajectories, [S] in the deflectometry system equation is updated

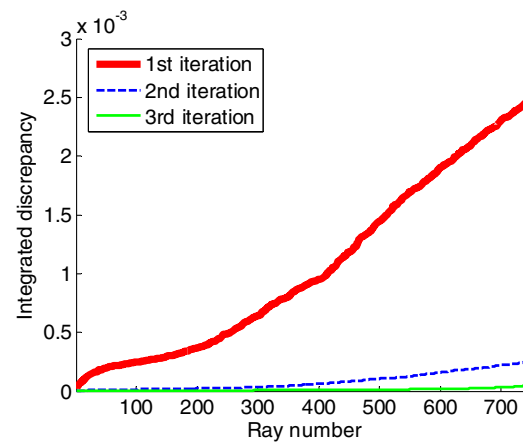


**Fig. 10.** Progressive improvement in the error metrics evaluated for individual rays after three iterations of refining ray trajectories.

and a new solution is calculated in the usual manner. This process is repeated until consistency in the solution is achieved.

It is useful to define an error metric for quantifying inconsistencies in the approximate trajectories assumed during reconstruction. A natural choice is the integrated absolute difference between the initial trajectory and the traced trajectory, i.e.,

$$\Delta = \int_a^b |y_{\text{trace}}(x) - y_{\text{initial}}(x)| dx, \quad (13)$$

where  $y_{\text{trace}}(x)$  is the trajectory obtained from a ray trace through the reconstructed index field and  $y_{\text{initial}}(x)$  is the trajectory assumed in the computation of [S] prior to system inversion. Following the corrective procedure outlined above, progressive improvement in the linear system description of deflectometry measurements is apparent after each iteration and consistency in the solution is achieved after just three iterations, as shown in Fig. 10, where the interrogating rays are sorted in ascending order based on their error metric to prevent coincidental patterns from developing in the plot.

In this simulation, the overall RMS index error relative to the test index field did not show a discernible improvement, but a notable difference between the reconstructed index fields in the first and last iterations of the procedure was observed (RMS difference of  $1.96 \times 10^{-4}$  refractive index units). This indicates that the path dependence of the system was not a significant contributor to the reconstruction error observed in Section 4.B. Furthermore, this result justifies our initial assumption used for decoupling ray trajectories from the index field and linearizing the system in measuring practical GRIN elements.

## 7. CONCLUSION

Using a simplifying assumption that decouples the trajectories of interrogating rays from the index field, a linear system description can be formulated for the inverse problem of solving a 2-D index field from boundary value measurements of ray position and slope. Under this assumption, ray trajectories can instead be approximated from measured (or simulated)

boundary values, and each deflectometry path integral can be expressed as a linear combination of the system's DoFs. These DoFs constitute Cartesian vector components of the index gradient field at discrete locations and are obtained through a numerical algorithm that can reliably invert sparse and ill-conditioned linear systems. The resulting gradient vector field can then be integrated to reconstruct the index field to within an unknown constant, which can only be identified with an additional measurement such as the index at some location. Using this approach, we were able to reconstruct a 2-D test index field using boundary values of ray position and ray slope obtained from a numerical ray trace, where the resulting RMS index error is below 0.5% of the index range.

To assess the sensitivity of the reconstruction process to measurement error, we introduced artificial Gaussian noise to the measured boundary values (obtained through simulation) and observed regimes in the noise level where one of three identified error mechanisms (quantization noise, base-line inversion sensitivity, and trajectory dependence) was dominant in contributing to the overall reconstruction error. In addition, we examined the limitations of the numerical inversion method by reconstructing the index field with varying amounts of data redundancy as well as angular coverage and testing the impact of system conditioning on inversion accuracy. Taking advantage of the system's resilience to slight variations in the ray trajectories, a numerical ray trace was performed on reconstructions of the index field to improve approximate trajectories. The end result enforces the dependence of ray trajectories on the index field so that the optimized solution is consistent with the principles of geometric optics.

The basic inversion procedure described in this paper employed internal ray positions and angles, and we required additional measurements of the index of refraction across the entrance and exit surfaces (e.g., by a refractometer) to extend the method to external rays. In the future, we plan on exploring methods of reconstructing the index field directly from *externally* measured ray slopes so that the refractive index along the boundaries of the GRIN element will not be needed to invert the system.

Finally, the rectangular geometry of the test field described in this paper was chosen simply to demonstrate the measurement procedure, and the method can be readily adapted to more complex geometries. In addition, the measurement principles are fully generalizable to three-dimensional GRIN elements.

## APPENDIX A

Equation (5) can be deduced from Eq. (3) as follows. The first derivative with respect to arc length variable  $s$  in terms of Cartesian coordinates is

$$\frac{d}{ds} = \frac{dx}{ds} \frac{d}{dx} = f \frac{d}{dx},$$

where

$$f = \frac{dx}{ds} = \frac{dx}{\sqrt{dx^2 + dy^2}} = \left[ 1 + \left( \frac{dy}{dx} \right)^2 \right]^{-1/2}$$

using the fact that  $ds^2 = dx^2 + dy^2$ . The second derivative is then

$$\frac{d^2}{ds^2} = f \frac{d}{dx} \left( f \frac{d}{dx} \right) = f \frac{df}{dx} \frac{d}{dx} + f^2 \frac{d^2}{dx^2}.$$

Rewriting Eq. (3) in scalar form, we have

$$\frac{dn}{ds} \frac{dx}{ds} + n \frac{d^2x}{ds^2} = \frac{\partial n}{\partial x}, \frac{dn}{ds} \frac{dy}{ds} + n \frac{d^2y}{ds^2} = \frac{\partial n}{\partial y}.$$

From the first scalar equation, we find that

$$\left( f \frac{dn}{dx} \right) \left( f \frac{dx}{dx} \right) + n \left( f \frac{df}{dx} \frac{dx}{dx} + f^2 \frac{d^2x}{dx^2} \right) = \frac{\partial n}{\partial x},$$

$$f^2 \frac{dn}{dx} = \frac{\partial n}{\partial x} - n f \frac{df}{dx},$$

where we have used  $\frac{dx}{dx} = 1$  and  $\frac{d^2x}{dx^2} = 0$ . The second scalar equation becomes

$$\left( f \frac{dn}{dx} \right) \left( f \frac{dy}{dx} \right) + n \left( f \frac{df}{dx} \frac{dy}{dx} + f^2 \frac{d^2y}{dx^2} \right) = \frac{\partial n}{\partial y},$$

$$\frac{dy}{dx} f^2 \frac{dn}{dx} + n \left( f \frac{df}{dx} \frac{dy}{dx} + f^2 \frac{d^2y}{dx^2} \right) = \frac{\partial n}{\partial y}.$$

Substituting the result for  $f^2 \frac{dn}{dx}$  from the first scalar equation into the equation above, canceling terms, and dividing by  $n$  yields Eq. (5):

$$\frac{dy}{dx} \frac{\partial n}{\partial x} - \frac{dy}{dx} n f \frac{df}{dx} + n f \frac{df}{dx} \frac{dy}{dx} + n f^2 \frac{d^2y}{dx^2} = \frac{\partial n}{\partial y},$$

$$\frac{\partial w}{\partial y} - \frac{\partial w}{\partial x} y' = \frac{y''}{1 + (y')^2},$$

where  $w = \ln(n)$  is the logarithmic refractive index.

## APPENDIX B

It is useful to switch to relative coordinates to illustrate the relationship between the gradient of  $w(x, y)$  and the angular deflection of a ray propagating through  $w(x, y)$ . If we define the  $x$  axis parallel to the ray at a particular point of interest, we have  $y' = 0$  in the final expression from Appendix A, which then simplifies to

$$\frac{\partial w}{\partial y} = y'',$$

where  $y$  is taken to be the direction normal to the ray in relative coordinates. Hence, the index field's directional derivative along the normal of the ray trajectory induces a local curvature in the ray's path. Rewriting  $y''$  as  $\frac{d}{dx} y'$  results in the differential

$$\Delta y' = \frac{\partial w}{\partial y} \Delta x.$$

Constructing a right triangle between the quantities  $\Delta x$ ,  $\Delta y$ , and  $\Delta s$  as seen in Fig. 11, we have the trigonometric relation

$$\tan(\Delta\theta) \approx \Delta\theta = \frac{\Delta y}{\Delta x} = \Delta y',$$

where  $\Delta\theta$  can be interpreted as angular deflection from the ray's current direction due to the local index gradient.

An explicit expression of  $\Delta\theta$  in terms of  $\Delta s$  is desired since it allows for a straightforward computation of the overall path

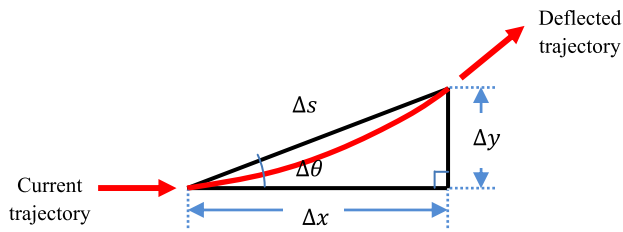


**Fig. 11.** Geometry of angular deflection from a ray's current trajectory.

integral. This is achieved with the first-order approximation  $\cos(\Delta\theta) = \frac{\Delta x}{\Delta s} \approx 1$ , where the differential angular deflection  $\Delta\theta$  is assumed to be small, such that

$$\Delta\theta \approx \Delta y' = \frac{\partial w}{\partial y} \Delta x \approx \frac{\partial w}{\partial y} \Delta s,$$

where we have made the substitution  $\Delta x \approx \Delta s$ . Noting that  $y$  is the direction normal to the ray trajectory and switching back to laboratory coordinates, the differential above can be written as

$$\Delta\theta = \vec{\nabla} w \cdot \hat{n} \cdot \Delta s = \left[ -\frac{\partial w}{\partial x} \sin(\theta) + \frac{\partial w}{\partial y} \cos(\theta) \right] \Delta s,$$

where  $\hat{n} = -\sin(\theta)\hat{i} + \cos(\theta)\hat{j}$  is the unit vector normal to the ray and  $\vec{\nabla} w = \frac{\partial w}{\partial x}\hat{i} + \frac{\partial w}{\partial y}\hat{j}$  is the gradient of the logarithmic index field.  $\theta$  is the angle of the ray relative to the (laboratory)  $x$  axis such that  $\tan(\theta) = y'$ .

## APPENDIX C

We integrate a 2-D gradient vector field by inverting the discrete gradient operator composed of linear algebraic equations used to compute the partial derivatives from the logarithmic index field  $w$ . For instance, the central difference is used at interior grid points, i.e.,

$$\frac{\partial w}{\partial x} \Big|_{i,j} = \frac{1}{2\Delta_x} (w_{i+1,j} - w_{i-1,j}), \quad \frac{\partial w}{\partial y} \Big|_{i,j} = \frac{1}{2\Delta_y} (w_{i,j+1} - w_{i,j-1}),$$

where  $\Delta_x$  is the separation between grid points along  $x$  and  $\Delta_y$  is the separation in  $y$ . For leading-edge grid points, we take the forward difference while the backward difference is used for trailing-edge points. These algebraic equations are assembled into a sparse matrix describing the gradient operator, whose inverse can be obtained using standard numerical methods. We then use the inverse operator to compute the logarithmic index  $w(x, y)$  from its partial derivatives, e.g.,

$$[\nabla]^{-1} \cdot \vec{\delta} = \vec{w}_1 + w_0,$$

where  $[\nabla]$  is the discrete gradient operator and  $\vec{\delta}$  is the partial derivative column vector from Eq. (12), which has presumably been solved from inverting the deflectometry system equation. The integration constant  $w_0$  can be identified with additional information such as the index at some location, and the column vector  $\vec{w}_1$  represents the potential function  $w_1(x, y)$  defined on the same grid as the partial derivative fields, whose discrete elements are lexicographically ordered into  $\vec{w}_1$ . In cases in

which  $\vec{\delta}$  does not describe a conservative gradient field, the inverse operator optimizes  $w_1$  so that discrepancies between  $\nabla w_1$  and the partial derivative fields in  $\vec{\delta}$  are minimized in the least squares sense.

DARPA (HQ0034-14-D-0001).

This work was funded by DARPA (contract HQ0034-14-D-0001). The views, opinions, and/or findings contained in this article are those of the authors and should not be interpreted as representing the official views or policies of the Department of Defense or the U.S. Government. This document is approved for public release, distribution unlimited.

## REFERENCES

1. D. T. Moore, "Gradient-index optics: a review," *Appl. Opt.* **19**, 1035–1038 (1980).
2. J. Teichman, J. Holzer, B. Balko, B. Fisher, and L. Buckley, "Gradient index optics at DARPA," IDA Document D-5027 (Institute for Defense Analyses, 2013), [https://www.ida.org/~media/Corporate/Files/Publications/IDA\\_Documents/STD/D-5027-FINAL.pdf](https://www.ida.org/~media/Corporate/Files/Publications/IDA_Documents/STD/D-5027-FINAL.pdf).
3. P. Sinai, "Correction of optical aberrations by neutron irradiation," *Appl. Opt.* **10**, 99–104 (1971).
4. M. A. Pickering, R. L. Taylor, and D. T. Moore, "Gradient infrared optical material prepared by a chemical vapor deposition process," *Appl. Opt.* **25**, 3364–3372 (1986).
5. S. Ohmi, H. Sakai, Y. Asahara, S. Nakayama, Y. Yoneda, and T. Izumitani, "Gradient-index rod lens made by a double ion-exchange process," *Appl. Opt.* **27**, 496–499 (1988).
6. B. Messerschmidt, T. Possner, and R. Goering, "Colorless gradient-index cylindrical lenses with high numerical apertures produced by silver-ion exchange," *Appl. Opt.* **34**, 7825–7830 (1995).
7. S. P. Wu, E. Nihei, and Y. Koike, "Large radial graded-index polymer," *Appl. Opt.* **35**, 28–32 (1996).
8. J. H. Liu, P. C. Yang, and Y. H. Chiu, "Fabrication of high-performance, gradient-refractive-index plastic rods with surfmer-cluster-stabilized nanoparticles," *J. Appl. Polym. Sci.* **44**, 5933–5942 (2006).
9. J. H. Liu and Y. H. Chiu, "Process equipped with a sloped UV lamp for the fabrication of gradient-refractive-index lenses," *Opt. Lett.* **34**, 1393–1395 (2009).
10. A. C. Urness, K. Anderson, C. Ye, W. L. Wilson, and R. R. McLeod, "Arbitrary GRIN component fabrication in optically driven diffusive photopolymers," *Opt. Express* **23**, 264–273 (2015).
11. G. Beadie, E. Fleet, A. Rosenberg, P. A. Lane, J. S. Shirk, A. R. Kamdar, M. Ponting, A. Hiltner, and E. Baer, "Gradient index polymer optics," *Proc. SPIE* **7061**, 706113 (2008).
12. S. Ji, K. Yin, M. Mackey, A. Bristler, M. Ponting, and E. Baer, "Polymeric nanolayered gradient refractive index lenses: technology review and introduction of spherical gradient refractive index ball lenses," *Opt. Eng.* **52**, 112105 (2013).
13. C. Wang and D. L. Shealy, "Design of gradient-index lens systems for laser beam reshaping," *Appl. Opt.* **32**, 4763–4769 (1993).
14. R. N. Zahreddine, R. S. Lepkowitz, R. M. Bunch, E. Baer, and A. Hiltner, "Beam shaping system based on polymer spherical gradient refractive index lenses," *Proc. SPIE* **7062**, 706214 (2008).
15. D. Lin and J. R. Leger, "Numerical gradient-index design for coherent mode conversion," *Adv. Opt. Technol.* **1**, 195–202 (2012).
16. A. J. Barnard and B. Ahlborn, "Measurement of refractive index gradients by deflection of a laser beam," *Am. J. Phys.* **43**, 573–574 (1975).
17. O. Wiener, "Darstellung gekrummter lichtstrahlen und verwerthung derselben zur untersuchung von diffusion and wärmeleitung," *Annu. Rev. Phys. Chem.* **285**, 105–149 (1893).
18. Z. Bodnar and F. Ratajczyk, "Some remarks concerning optical glass heterogeneity measurement with the help of the autocollimation method," *Appl. Opt.* **4**, 351–354 (1965).

19. D. T. Moore and D. P. Ryan, "Measurement of the optical properties of gradient index materials," *J. Opt. Soc. Am.* **68**, 1157–1166 (1978).
20. P. Meemon, J. Yao, K.-S. Lee, K. P. Thompson, M. Ponting, E. Baer, and J. P. Rolland, "Optical coherence tomography enabling non-destructive metrology of layered polymeric GRIN material," *Sci. Rep.* **3**, 1709 (2013).
21. D. Lin, J. R. Leger, M. Kunkel, and P. McCarthy, "One-dimensional gradient-index metrology based on ray slope measurements using a bootstrap algorithm," *Opt. Eng.* **52**, 112108 (2013).
22. D. W. Sweeney and C. M. Vest, "Reconstruction of three-dimensional refractive index fields from multidirectional interferometric data," *Appl. Opt.* **12**, 2649–2664 (1973).
23. T. Yuasa, A. Maksimenko, E. Hashimoto, H. Sugiyama, K. Hyodo, T. Akatsuka, and M. Ando, "Hard-x-ray region tomographic reconstruction of refractive-index gradient vector field: imaging principles and comparisons with diffraction-enhanced-imaging-based computed tomography," *Opt. Lett.* **31**, 1818–1820 (2006).
24. S. Gasilov, A. Mittone, E. Brun, A. Bravin, S. Grandl, A. Mirone, and P. Coan, "Tomographic reconstruction of the refractive index with hard x-rays: an efficient method based on the gradient vector-field approach," *Opt. Express* **22**, 5216–5226 (2014).
25. P. L. Chu, "Nondestructive measurement of index profile of an optical-fibre preform," *Electron. Lett.* **13**, 736–738 (1977).
26. A. W. Lohmann, R. G. Dorsch, D. Mendlovic, Z. Zalevsky, and C. Ferrerira, "Space-bandwidth product of optical signals and systems," *J. Opt. Soc. Am. A* **13**, 470–473 (1996).
27. W. H. Southwell, "Ray tracing in gradient-index media," *J. Opt. Soc. Am.* **72**, 908–911 (1982).
28. Y. Nishidate, T. Nagata, S.-Y. Morita, and Y. Yamagata, "Ray-tracing method of isotropic inhomogeneous refractive-index media from arbitrary discrete input," *Appl. Opt.* **50**, 5192–5199 (2011).
29. C. C. Paige and M. A. Saunders, "LSQR: an algorithm for sparse linear equations and sparse least squares," *AMC Trans. Math. Softw.* **8**, 43–71 (1982).